

Patch2Loc: Learning to Localize Patches for Unsupervised Brain Lesion Detection

Hassan Baker, *Graduate Student, IEEE*, and Austin J. Brockmeier, *Senior Member, IEEE*

Abstract—Detecting brain lesions as abnormalities observed in magnetic resonance imaging (MRI) is essential for diagnosis and treatment. In the search of abnormalities, such as tumors and malformations, radiologists may benefit from computer-aided diagnostics that use computer vision systems trained with machine learning to segment normal tissue from abnormal brain tissue. While supervised learning methods require annotated lesions, we propose a new unsupervised approach (Patch2Loc) that learns from normal patches taken from structural MRI. We train a neural network model to map a patch back to its spatial location within a slice of the brain volume. During inference, abnormal patches are detected by the relatively higher error and/or variance of the location prediction. This generates a heatmap that can be integrated into pixel-wise methods to achieve finer-grained segmentation. We demonstrate the ability of our model to segment abnormal brain tissues by applying our approach to the detection of tumor tissues in MRI on T2-weighted images from BraTS2021 and MSLUB datasets and T1-weighted images from ATLAS and WMH datasets. We show that it outperforms the state-of-the-art in unsupervised segmentation. The codebase for this work can be found on our GitHub page.

Index Terms—Anomaly detection, Convolutional neural networks, Computer aided diagnosis, Machine learning, Magnetic resonance imaging, Neuropathology, Neuroradiology, Self-supervised learning, Tumors

I. INTRODUCTION

Detecting and localizing abnormal brain tissue through non-invasive neuroimaging is a critical medical task with profound implications for patients' well-being and overall quality of life. Early detection and intervention can mitigate severe consequences in cases such as incipient brain tumors or cortical malformations, which are associated with drug-resistant pediatric epilepsy [1]. The intricate structural complexity of the brain necessitates the expertise of neurologists and radiologists for accurate diagnosis. The development of computer-aided diagnostics at an expert level is motivated by the shortage of neuroradiologists [2].

Magnetic resonance imaging (MRI) has emerged as a reliable modality for detecting lesions within the brain [3]–[5]. MRI offers the distinct advantage of being radiation-free and non-invasive and different sequences can produce various tissue contrasts. In recent years, significant strides have been made in leveraging machine learning, particularly deep learning techniques for computer vision [6] to automate the detection and localization of abnormal brain tissues in neuroimages.

Methods generate abnormality scores at the pixel or voxel-level that can be thresholded to segment images abnormal and normal regions. This progress is largely attributable to the availability of extensive datasets and advanced deep learning methodologies.

While models trained with supervision may be expected to exhibit superior performance, they require extensive annotations delineating the anomalies. However, the release of detailed annotations is limited, especially for rare abnormalities [7], [8]. This motivates the improvement of unsupervised learning methods that use only putative normal images that can then be applied for abnormal brain tissue detection. Possibly using a minimal set of labeled images for hyper-parameter selection.

As discussed in Section V, state-of-the-art methods use autoencoders, denoising autoencoders, and diffusion models learn to reconstruct or denoise normal images based on the typical structure, such that the reconstructions of abnormal portions of images is closer to typical structure and the reconstruction errors highlight abnormalities. In particular, denoising diffusion probabilistic models (DDPMs) have recently outperformed other generative and restoration-based approaches for unsupervised abnormality detection [9]–[13]. The key idea is to train a DDPM on normal brain MRI volumes (3D images) or slices (2D image taken from the 3D image of the brain). Since the model learns the patterns of normal brains, if it is fed with slices contain abnormal regions, it inpaints abnormal regions with normal patterns. The reconstruction error, typically measured as the pixel-wise difference between the original and reconstructed images, serves as a heatmap for potential anomalies, with higher errors indicating regions more likely to contain abnormalities.

Despite their effectiveness, DDPMs suffer from the noise paradox [9], [14], where the level of added noise during inference significantly impacts performance: higher noise levels remove more anomalies but increase false positives due to over-inpainting of normal tissues. This trade-off complicates the detection process and limits DDPM's reliability in clinical settings. Furthermore, DDPMs and the vast majority of existing unsupervised abnormality segmentation methods for brain MRI rely on processing entire slices. Thus, these methods detect localized lesions from a “global” context. In contrast, analyzing local patterns in isolation, given their location, may provide more focused detection of abnormalities.

With this motivation, we introduce **Patch2Loc**, a novel framework tailored for achieving unsupervised abnormality segmentation in neuroimaging. We create a self-supervised task, predicting the location of a patch, such that given the true location the differences and uncertainty with the prediction can identify local anomalies.

H. Baker is affiliated with the Department of Electrical and Computer Engineering, University of Delaware, Newark, DE, 19716 USA (e-mail: bakerh@udel.edu)

A. J. Brockmeier is affiliated with the Department of Electrical and Computer Engineering, Department of Computer and Information Sciences, University of Delaware, Newark, DE, 19716 USA (e-mail: ajbrock@udel.edu)

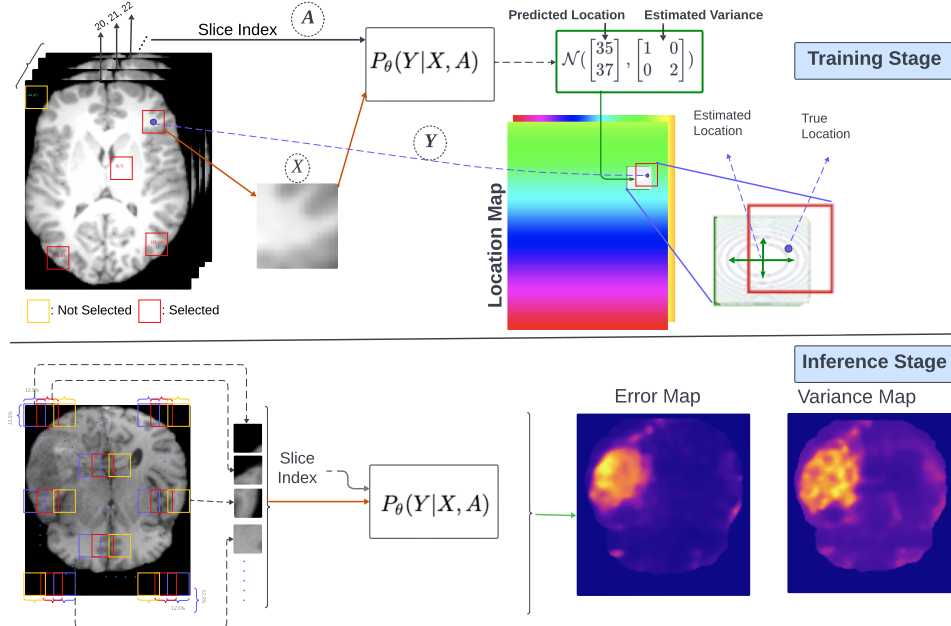


Fig. 1. Schematic diagram for Patch2Loc. (Top) Training stage: A randomly selected patch from a normal MRI slice (patches with less than 20% of its content as brain tissues, as in the yellow patch, are rejected) is paired with its two-dimensional location Y and slice index A . The relationship between the image patch, slice, and its location is modeled as a conditional distribution $P_\theta(Y|X, A)$ using a 2D Gaussian distribution defined by the mean and variance of each coordinate that are functions of the patch and slice index. (Bottom) Inference stage: Overlapping patches with a fixed stride are extracted as in convolution from an MRI slice and the model is applied to each patch. The norm of the difference between the model's predicted mean and the patch's true location creates an error map. Likewise, the sum of the variances create a variance map. Together the norm of the error and variance can identify anomalous patches.

A. Main Contributions

Our approach offers several key advantages:

- 1) **Spatially-Aware Local Feature Learning:** Patch2Loc learns to predict the spatial origin of a given patch within the brain. By encoding local anatomical and tissue structure patterns from normal tissue patches, the model can effectively distinguish abnormal patches based on deviations in location prediction.
- 2) **Uncertainty-Guided Anomaly Detection:** The variance in Patch2Loc's predictions serves as an uncertainty estimate, enabling more robust abnormality detection. By combining location error and uncertainty, we derive an enhanced abnormality score that improves detection performance.
- 3) **Minimal Hyperparameter Dependence:** Unlike DDPM-based methods, which require hyperparameter tuning (e.g., noise level selection), Patch2Loc is self-supervised and adaptable. The most anomalous patches can be found by the abnormality score.

By shifting the focus to local features and leveraging self-supervised learning, Patch2Loc's abnormality score is intuitive and easy to interpret and avoidance of extensive hyperparameter tuning and labeled data increases clinical applicability.

II. METHODOLOGY

The idea underlying Patch2Loc is that there is a strong relationship between patch content and location, due to the

local patterns in structural neuroimages, that is used by neuroradiologists when identifying structural abnormalities. With sufficient sampling across the population, this relationship can be modeled using machine learning. As each brain has slightly different sizes, the images are first registered using rigid transformation. Fig. 1 shows a summary schematic diagram for methodology behind Patch2Loc.

A. Problem Formulation

Let $(Y_1, Y_2, A) \in [0, 100]^3$ denote the 3D location of a rectangular image patch $X \in \mathcal{X} \subset \mathbb{R}_{\geq 0}^{S_1 \times S_2}$ within the brain taken at the 2D location $Y = (Y_1, Y_2) \in [0, 100]^2$ from the slice located at $A \in [0, 100]$. The coordinates are percentages of the patch's location in absolute coordinates (L_1, L_2, L_3) relative to the brain volume's spatial extent along each axis (E_1, E_2, E_3) : $Y_1 = 100 \cdot \frac{L_1}{E_1}$, $Y_2 = 100 \cdot \frac{L_2}{E_2}$, and $A = 100 \cdot \frac{L_3}{E_3}$. With registered brain scans, the spatial extents E_1, E_2, E_3 are constant for all scans. Each 2D patch is rectangular with an absolute size of $S_1 \times S_2$ chosen based on a fixed relative proportion $r = \frac{S_1}{E_1} = \frac{S_2}{E_2}$. The choice of r controls the patch's coverage.

The patch and location can be described as continuous random variables jointly distributed $(X, Y, A) \sim P$. Intuitively, $P(X|Y_1 = y_1, Y_2 = y_2, A = a)$ is the distribution of images at a particular location (y_1, y_2, a) , but this is a high-dimensional distribution that is difficult to model. To capture the shared information between the image patch and its location, we

model the conditional distribution $P(Y|X, A)$, which is two dimensional. For simplicity, we model this as a 2D Gaussian distribution,

$$P_\theta(Y|X, A) = \mathcal{N}(\mu^\theta(X, A), \Sigma^\theta(X, A)), \quad (1)$$

where $\mu^\theta(X, A)$ is the 2D mean and $\Sigma^\theta(X, A)$ is the covariance matrix, both are functions of the patch X and the slice location A , parameterized by θ . To further simplify the model, we consider a diagonal covariance matrix described by the variance of the two coordinates. The model is then $Y_i|X, A \sim \mathcal{N}(\mu_i^\theta(X, A), \Sigma_{ii}^\theta(X, A)), \quad i \in \{1, 2\}$.

The functions describing the conditional mean and variances μ^θ and Σ^θ are modeled using a neural network with parameters $\theta = (\theta_0, \theta_m, \theta_v)$, where θ_0 are the parameters of the shared patch encoder $\phi : \mathcal{X} \rightarrow \mathbb{R}^d$, θ_m are the parameters of the mean prediction head $\tilde{\mu}$, such that $\mu^\theta(X, A) = \tilde{\mu}(\phi(X), A) \in \mathbb{R}^2$, and θ_v are the parameters particular to the log-variance head $\tilde{\varsigma}$, such that $\varsigma^\theta(X, A) = \tilde{\varsigma}(\phi(X), A) \in \mathbb{R}^2$ and $\Sigma_{ii}^\theta(X, A) = \exp(\varsigma_i^\theta(X, A)), \quad i \in \{1, 2\}$.

B. Loss Function

The model parameters could be optimized to minimize the negative-log likelihood (NLL)

$$\theta^* \in \operatorname{argmin}_\theta \mathbb{E}_{(X, Y, A) \sim P} [-\log P_\theta(Y|X, A)]. \quad (2)$$

However, using NLL for estimating a model of both the mean and the variance is problematic as the component of the loss with respect to the mean estimates are scaled by the variance estimates,

$$-\log P_\theta(Y|X, A) \propto \sum_{i=1}^2 \frac{|Y_i - \mu_i^\theta(X, A)|^2}{\exp(\varsigma_i^\theta(X, A))} + \varsigma_i^\theta(X, A), \quad (3)$$

which causes convergence to local minima with poor performance [15], [16]. Hence, we adapt the β -NLL loss proposed in the work by [16] that scales each dimension of the loss by the variance estimate taken to the β th power, $\beta \in (0, 1]$,

$$\sum_{i=1}^2 [\exp(\varsigma_i^\theta(X, A))]^\beta \left(\frac{|Y_i - \mu_i^\theta(X, A)|^2}{\exp(\varsigma_i^\theta(X, A))} + \varsigma_i^\theta(X, A) \right), \quad (4)$$

where $[\cdot]$ indicates the stop-gradient operation such that gradients are not taken with respect to this scaling. This scaling mitigates the issue of the gradient of the loss with respect to the mean depending on the variance estimate.

C. Abnormality Scores

To detect abnormalities with Patch2Loc, we calculate an abnormality score from both location prediction error and the variance estimates, after log transformation. The log of the squared error is calculated as $\log(\|Y - \mu^\theta(X, A)\|_2^2)$. The log-variance is calculated as $\log(\exp(\varsigma_1^\theta(X, A)) + \exp(\varsigma_2^\theta(X, A)))$. We define the abnormality score as the sum of the log-squared error and log-variance, which is the β -NLL loss (4) for $\beta = 1$.

D. Model Details

While the Patch2Loc task can be applied to different anatomical orientations for the slices, we consider axial slices, such that A is proportional to the location of the slice along the vertical dimension (bottom to top of the brain). We select $r = 12.5\%$ for the proportion of the axial slice's width and length. Ideally, the smaller the patch, the more precise the resulting heatmap would be. However, in development we found that smaller patch sizes deteriorates Patch2Loc's performance since the patches are more ambiguous. When the patch size is too small, the inherent structural symmetry of the brain causes patches from different locations to appear similar, making it challenging for Patch2Loc to distinguish between them effectively.

For the encoding model $\phi : \mathbb{R}_{\geq 0}^{S_1 \times S_2} \rightarrow \mathbb{R}^d$, which serves as a common backbone, we use ResNet-18 [17], producing a shared latent feature vector with dimension $d = 512$. Since the patch size are small (i.e., $S_1 \times S_2 = 24 \times 24$), we replace the ResNet-18 first convolution layer with a kernel of size 3 instead of 7. The latent vector from the backbone $\phi(X) \in \mathbb{R}^d$ is added to a sinusoidal positional encoding of the slice coordinate A [18]. This representation is input to two separate branches for the mean $\tilde{\mu} : \mathbb{R}^d \rightarrow \mathbb{R}^2$ and the log-variance $\tilde{\varsigma} : \mathbb{R}^d \rightarrow \mathbb{R}^2$. Each branch consists of four fully-connected (FC) layers with output dimensions 128, 64, 32, and a batch normalization layer and a rectified linear unit (ReLU) activation function between each two linear layers, followed by a linear layer to the two-dimensional outputs. For the β -NLL loss in (4), we choose the suggested value of $\beta = 0.5$ [16]. We confirmed that using NLL as a loss directly results in a local minimum where the model produces a high variance estimate and the mean has a high error.

E. Convolutional Approach for Pixel-level Detection

To perform pixel-level abnormality detection, we employ Patch2Loc in a convolutional manner. Specifically, for each slice we feed overlapping patches with a specified stride into the Patch2Loc model. Subsequently, we utilize the Patch2Loc outputs, predicted mean and variance, along with the maps of the true coordinates sampled at the same stride to construct a scoring map. A stride of 1 results in a scoring map identical in size to the testing MRI image, albeit with increased computational demands. This is depicted in the bottom section of Fig. 1.

We define the pixel-wise abnormality score image, i.e., the heatmap, as $H \in \mathbb{R}^{\hat{m} \times \hat{n}}$, where: $\hat{m} = \lfloor \frac{m-1}{stride} \rfloor + 1, \hat{n} = \lfloor \frac{n-1}{stride} \rfloor + 1$. Here, m and n are the dimensions of the input slice after zero-padding according to the patch size to enable slices to be obtained up to the brain edges, and $stride$ is the step size used for computing the heatmap. Throughout all experiments, we use a stride of 1, meaning that the heatmap H retains the same dimensions as the input slice (i.e., $\hat{m} = m, \hat{n} = n$). If a larger stride is used ($stride > 1$), the heatmap H will have a lower resolution, but it can be upsampled (e.g., via interpolation) to match the input dimensions.

III. DATA

We preprocess the neuroimages by skull-stripping, registering each to the SRI atlas [19], resampling to a voxel dimension of 1 mm^3 , applying N4 bias-correction, applying the histogram standardization method proposed by [20], and finally, dividing each MRI image by its 98th percentile. The histogram standardization method in [20] uses statistics (e.g., quantiles and the second mode) obtained from a dataset. We use the training dataset to estimate these statistics, and then we standardize every image from all datasets using the same statistics.

For the training data, we use the IXI dataset, which contains MRI scans in both T1- and T2-weighted modalities for 560 subjects. Following the procedure outlined in [13], [21], a total of 158 samples are set aside for testing, while the remaining data is divided into five sets for cross-validation. Each set consists of 358 training samples and 44 validation samples.

For evaluation, we employ three different datasets: BraTS21 [22], [23] with 1152 subjects, and multiple sclerosis patients with lesion segmentation based (MSLUB) [24] with 30 subjects, white matter hyperintensity (WMH) [25] with 60 subjects, and Anatomical Tracings of Lesions After Stroke v2.0 (ATLAS) [26] with 955 subjects. The first two use T2-weighted and the last two use T1-weighted modality. These datasets represent different types of abnormal tissues. BraTS21 focuses on brain tumors with varying sizes and convex structures. MSLUB and WMH contain lesions from multiple sclerosis and white matter hyperintensities, respectively, which are relatively smaller and more scattered than tumors. ATLAS has small convex shaped abnormal tissues. Sample slices from these datasets, along with their ground truth abnormal tissue segmentation, are shown in Fig. 4.

A. Patch2Loc Training Details

For each training batch, we randomly select one slice from each of the 358 training subjects. From the combined pool of 358 slices, we uniformly sample 8096 patches. Patches are discarded if more than 80% of their pixels are background (i.e., $\geq 20\%$ brain tissue). This is depicted in the top section of the schematic diagram shown in Fig. 1, where the yellow outline patch in the top left corner are rejected due to their substantial empty content. This process defines a single batch, and Patch2Loc is trained for 15,000 such batches. Adam [27] is used as an optimizer with a learning rate 10^{-2} and other hyper-parameters are left as defaults. We use a single NVIDIA V100 GPU to train the model.

IV. RESULTS

We analyze the results in three parts: Firstly, we investigate the distributions of Patch2Loc’s location prediction errors and predicted variance, underlying the abnormality score, across normal and abnormal patches. Secondly, we qualitatively illustrate the performance of Patch2Loc on representative examples from each dataset. Finally, we quantitatively discuss the segmentation performance of Patch2Loc and we compare our results with benchmark and state-of-the-art (SOTA) methods [9], [12], [13], [21], [28]–[31]. We choose variety of methods that reflect different methodologies such as AE, VAE, GANs, and

diffusion models that have published results on these datasets. Performance is measured, following previous work, in terms of both average precision (area under the precision-recall curve) and the best possible Dice-coefficient (highest possible F1 score).

A. Abnormality Score Analysis

We first illustrate the operation of Patch2Loc by examining the predicted distribution (mean and variance) of patches extracted from the same spatial location across subjects. For patch-level analysis, we obtain a set of non-overlapping patches from the abnormal datasets across all slices and individuals. We categorize a patch as either normal if it contains less than 10% of abnormal tissues or abnormal if it comprises over 90% of abnormal tissues. Patches falling within the 10% to 90% abnormal tissue percentage range are separately analyzed. We compare Patch2Loc’s predictions for normal and abnormal patches drawn from the BraTS dataset in Fig. 2. For normal patches, we observe low uncertainty (i.e., smaller ellipses) and low error, as the predictions are tightly clustered around the true location. Conversely, for abnormal patches, the model exhibits higher uncertainty (i.e., larger ellipses) and greater prediction error, with the predicted means deviating significantly from the true location.

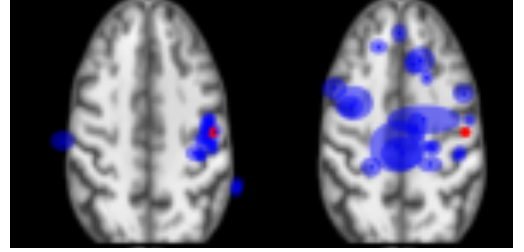


Fig. 2. Visualization of Patch2Loc’s output (blue ellipses) for patches captured from the same location (red dot) across different subjects in the BraTS dataset, overlaid on a representative T1-weighted registered slice (without abnormalities). (Left) Predictions of normal patches. (Right) Predictions of abnormal patches. The predicted Gaussian distribution is visualized as an ellipse, where the center represents the predicted mean, and the major and minor axes correspond to two standard deviations.

Fig. 3 shows kernel density estimates (KDEs) of Patch2Loc’s location prediction log-errors and predicted log-variance on normal and abnormal patches. Fig. 9 in the Appendix shows the results for the remaining datasets. There is a clear separation between the normal and abnormal patches in the space of log-error and log-variance although there is some overlap. This overlap occurs because Patch2Loc accurately predicts the location of abnormal patches with low variance. Such predictions are more likely when the abnormal patches are located at the edges of the brain, where Patch2Loc can utilize the surrounding empty space to make precise location predictions. This is mitigated by having overlapped patches as explained in Section II-E.

To investigate Patch2Loc on the partially abnormal patches (i.e., the patches that have abnormal content between 10% and 90%), we calculate the Spearman correlation between the abnormal content and log-error², log-variance, and the

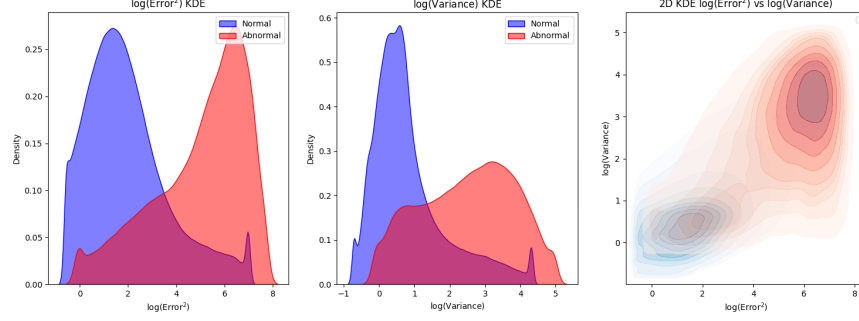


Fig. 3. From left to right: 1D KDE for log-error, and log-variance, and 2D KDE for log-error and log-variance for normal patches (blue) and abnormal patches (red) for the BraTS dataset.

abnormal score (i.e., their sum) for each dataset as shown in Table I. In all datasets, the abnormality score of the sum better correlates with the level of proportion of abnormal tissue compared to either squared-error or variance alone.

TABLE I
SPEARMAN CORRELATION (%) BETWEEN ABNORMALITY SCORES AND PATCHES ABNORMALITY CONTENT.

Dataset	log-error ²	log-variance	log-error ² + log-var
ATLAS	20%	18%	23%
BraTS	37%	34%	40%
MSLUB	15%	14%	17%
WMH	12%	11%	13%

B. Qualitative Analysis

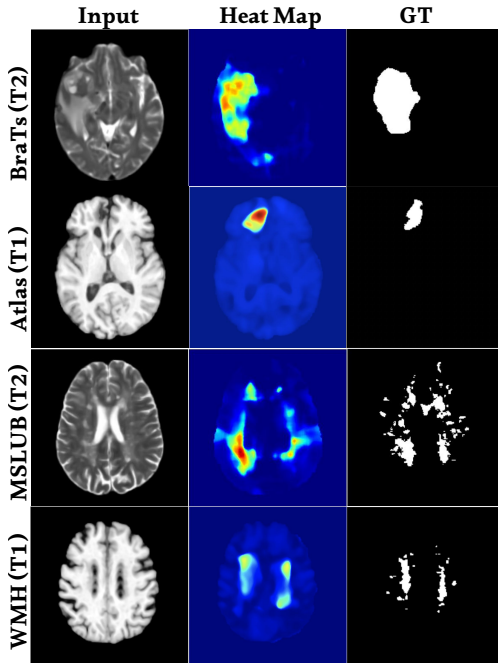


Fig. 4. Visualization of slices from BraTS, ATLAS, MSLUB, and WMH datasets (top to bottom). From left to right: the input slice, the heatmap (blue is low, red is the maximum), and the ground truth for abnormal tissues.

In Fig. 4, we present visualizations of MRI slices from the BraTS, ATLAS, MSLUB and WMH datasets, along with the corresponding heatmaps and ground truth annotations for abnormal tissues. While only one representative slice from each dataset are shown, they reflect a consistent pattern observed across both datasets. Additional visualizations are provided in the Appendix (Fig. 5 for BraTS, Fig. 7 for MSLUB, Fig. 6 for ATLAS, and Fig. 8 for WMH).

From these visualizations, we observe that the heatmaps spatially correspond to the ground truth abnormality regions. The correspondence for the BraTS is apparent. The abnormalities in BraTS are tumors, and patches from overlapping tumors will lack the normal anatomical structure necessary for accurate location prediction. In the case of MSLUB, the presence of normal tissue surrounding small and scattered abnormal regions provides contextual cues that may allow Patch2Loc to have correct location predictions. The same applies to WMH where the long but narrow abnormal structure also provide contextual cues. Likewise, in ATLAS, if the abnormal region is very small (e.g., in the first row in Fig. 6), it will go unpredicted. However, the presence of abnormalities within a patch may still cause the location prediction or increased variance in the prediction, such that Patch2Loc’s abnormality score does correlate with these smaller abnormalities. That is, Patch2Loc’s abnormality score is high due to in-distribution ambiguity, with large variance estimates, or out-of-distribution patches causing error in the location prediction, and a wide range of variance estimates. These different cases can be seen in the KDE plots as in Fig. 3 and Fig. 9. Finer grained out-of-distribution detection could be further enhanced by modeling the latent representations of a patch (see Section VII for discussion of future work.)

C. Segmentation Performance

We now consider the quantitative analysis of the pixel-wise segmentation performance of abnormalities for Patch2Loc on the BraTS, MSLUB, ATLAS, and WMH datasets. Following previous works, we compare Patch2Loc to benchmarks in Table II in terms of average precision and [Dice], which is the maximum Dice score possible per subject. We see that Patch2Loc often matches or outperforms the best performing method, with a wide margin for [Dice] on the WMH dataset.

TABLE II

COMPARISON OF THE EVALUATED MODELS WITH THE BEST RESULTS HIGHLIGHTED IN BOLD, AND SECOND BEST UNDERLINED. FOR ALL METRICS, THE MEAN \pm STANDARD DEVIATION ACROSS THE DIFFERENT FOLDS ARE REPORTED.

Model	BraTS21 (T2)		MSLUB (T2)		ATLAS (T1)		WMH (T1)	
	[DICE] [%]	AUPRC [%]	[DICE] [%]	AUPRC [%]	[DICE] [%]	AUPRC [%]	[DICE] [%]	AUPRC [%]
<i>Thresh</i> [29]	30.26	20.27	7.65	4.23	4.66	1.71	10.32	4.72
VAE [32]	33.12 \pm 1.12	25.74 \pm 1.37	8.10 \pm 0.18	4.48 \pm 0.18	15.63 \pm 0.73	11.44 \pm 0.5	7.60 \pm 0.28	3.86 \pm 0.40
SVAE [30]	36.43 \pm 0.36	30.3 \pm 0.45	8.55 \pm 0.11	4.8 \pm 0.09	10.32 \pm 0.53	6.84 \pm 0.44	7.18 \pm 0.07	2.97 \pm 0.06
AE [32]	36.04 \pm 1.73	28.8 \pm 1.72	9.65 \pm 0.97	5.71 \pm 0.80	14.04 \pm 0.6	10.16 \pm 0.53	7.34 \pm 0.08	3.43 \pm 0.14
DAE [33]	48.82 \pm 3.68	49.38 \pm 4.18	7.57 \pm 0.61	4.47 \pm 0.69	15.95 \pm 0.69	13.37 \pm 0.62	12.02 \pm 1.01	8.54 \pm 1.02
RA [34]	16.75 \pm 0.51	9.98 \pm 0.43	3.96 \pm 0.03	1.92 \pm 0.04	12.21 \pm 0.98	8.75 \pm 0.93	6.04 \pm 0.45	3.15 \pm 0.31
PHANES [31]	28.42 \pm 0.91	21.29 \pm 1.06	6.11 \pm 0.27	2.98 \pm 0.07	17.62 \pm 0.41	13.81 \pm 0.48	7.55 \pm 0.17	3.87 \pm 0.13
FAE [28]	44.59 \pm 2.19	43.63 \pm 0.47	6.85 \pm 0.65	3.85 \pm 0.08	17.76 \pm 0.16	13.91 \pm 0.10	8.81 \pm 0.38	4.77 \pm 0.26
DDPM [9]	50.27 \pm 2.67	50.61 \pm 2.92	9.71 \pm 1.29	6.27 \pm 1.58	20.18 \pm 0.58	17.77 \pm 0.47	12.06 \pm 0.97	8.89 \pm 0.89
pDDPM [13]	53.61 \pm 0.51	55.08 \pm 0.54	12.83 \pm 0.40	10.02 \pm 0.36	19.92 \pm 0.24	17.84 \pm 0.10	10.13 \pm 0.53	7.52 \pm 0.56
cDDPM [21]	56.30 \pm 1.25	58.82 \pm 1.56	14.04 \pm 1.16	10.97 \pm 1.17	24.22 \pm 1.10	22.22 \pm 1.15	11.59 \pm 0.93	9.26 \pm 1.07
Patch2Loc (Ours)	59.50 \pm 1.45	<u>55.40 \pm 1.30</u>	14.30 \pm 1.40	8.70 \pm 1.20	25.50 \pm 0.73	<u>22.00 \pm 1.70</u>	15.70 \pm 1.70	10.10 \pm 1.70

V. RELATED WORK

Unsupervised abnormality segmentation in neuroimaging has benefited from improving machine learning models ranging from autoencoders (AE), variational autoencoders (VAE) [32], generative adversarial neural networks (GANs) or discriminators as in GANs [35], transformers, and diffusion models. Nonetheless, a notable baseline is based on a simple threshold on the image histogram [29], which can exceed the performance of baseline methods for certain modalities.

Many approaches leverage AE or VAE in novel ways. An early work [36] introduced *ceVAE*, which combines variational and context autoencoders to compute abnormality scores from density and reconstruction error. Another work [37] uses a VAE with the abnormality score defined as the reconstruction error divided by the estimated variance. Rather than relying on squared error for training, another work [28] uses an AE architecture that reconstructs features obtained from a pretrained encoder using the Structural Similarity Index Measure (SSIM) as the loss function. SVAE [30] uses a VAE with transformers to capture the inter-slice dependencies and showed it can improve the results compared to 2D vanilla VAE. The RA method [34] uses an VAE with a cyclic loss and use the reconstruction error as abnormality score.

Previous studies, e.g., [11], [32], noted that AE and VAE methods suffer from blurry reconstructed images, which hinders their performance. Incorporating a discriminator as in a GAN can improve the reconstruction quality. However, methods incorporating GAN-losses suffer from training instability to the competition between the discriminator and decoder. Nonetheless, the work [38] proposed an adversarial autoencoder (AAE) that enforces a prior on the latent space and a cyclic objective for encoder consistency such that an image and its reconstruction are similar in the latent space. AnoVAGAN [39] is a variational autoencoder with spatially organized latent codes and a GAN loss.

Another approach is to iteratively restore an image to better match the normal data distribution, using the number of restoration steps as an abnormality score [40]. PHANES [31] uses a model to restore part of an MRI slice flagged by the RA method [34] to mitigate false positives within the flagged region.

One prior work [41] used a patch-based auto-encoder with a cycle consistency term and a discriminator to distinguish between the original image and its reconstruction, testing it on specific abnormal tissues. We identified it as the only approach leveraging local features for unsupervised abnormality segmentation in brain MRI. However, it suffers from instability due to adversarial training and difficulty in balancing multiple loss terms, which is challenging in unsupervised setting. The method was applied to detect infarcts, but it was not applied to abnormality segmentation and was not compared against any existing work. Thus, it is questionable if patch-level reconstruction would be competitive compared to slice-level reconstructions.

While the aforementioned works advanced unsupervised abnormality detection for neuroimages, all are outperformed by a significant margin by using a denoising autoencoder (DAE) [33], which learns to remove correlated noise added to the input images during training. DAE outperformed GAN and VAE approaches, achieving higher Dice score and average precision.

A promising work [11] introduced a combined vector-quantized variational autoencoder to learn spatial latent representation for brain slices and then used it to train an autoregressive transformer that operates on patches of the latent representation using different raster orders. Unfortunately, the results are not comparable as they are limited to the FLAIR modality, with 15,000 normal scans sourced from the UK Biobank (UKB) dataset, which is not freely available, and the method was not tested with other modalities or datasets. It should be noted that the IXI dataset used for training in our benchmark does not have FLAIR modality.

While not used for unsupervised abnormality segmentation, one prior work [42] resembles Patch2Loc’s self-supervised location prediction task, creating a 3D version of a previous context-dependent self-supervised task of predicting a patch’s relative location with respect to a context patch as a classification problem [43]. The task consists of predicting the discrete relative location of a 3D patch among the $3 \times 3 \times 3 - 1$ possible grid locations surrounding a center patch. Essentially, the goal is to infer the relative location of one patch with respect to center patch as context. The performance for unsupervised

abnormality segmentation was not benchmarked as the method was applied to create a latent representation via a backbone network that improves subsequent supervised segmentation performance [42]. Patch2Loc is distinguished by its use of continuous locations without the need of a center patch as context, as the slice index is sufficient context in registered brain images.

A. Denoising Diffusion Probabilistic Models

Many of the top performing methods for unsupervised abnormality detection use denoising diffusion probabilistic models (DDPM). Unless stated otherwise, all methods use the abnormality score as the absolute reconstruction error between input and denoised ones. One of the first works to use DDPM [9] also proposed learning to denoise simplex noise instead of Gaussian noise to enhance performance. While this empirically works, how this matches the fundamental assumptions of diffusion processes is not clear. Specifically, simplex noise is procedurally generated, and is not described by a random process. In contrast, a diffusion model's forward process is described by a Markov chain, with a Markov transition kernel [44], typically described by adding Gaussian noise, but the Markov chain can also be described by a Bernoulli transition kernel [44]. Without a known Markov transition kernel, the derivation of the DDPM formulation [45] may not be applicable to simplex noise, since the Gaussian assumption is exploited to define the forward process posterior mean. Nonetheless, ignoring the validity the DDPM formulation essentially defines a training regime for denoising across different signal-noise levels, where longer times correspond to higher noise regimes. During inference, denoising is performed from the initially high noise regime, then new simplex noise is applied at decreasing noise levels, and the process is repeated.

Another work [10] trained diffusion models on the learned spatial latent features and during inference time the abnormal features are inpainted with normal ones. Then the reconstructed image is obtained using the denoised spatial latent features that are fed to a decoder. Although their work showed an impressive performance for head CT, for brain MRI, their work did not exceed their earlier work [11]. This was extended by another work [46] that leveraged a diffusion model for cyclic translations between different modalities and implemented a conditional model, akin to a restoration-based approach. While the model shows superior performance compared to all other techniques mentioned above it requires different modalities.

Similarly, another work [14] introduced an iterative inpainting technique to address the noise paradox in order to mitigate the false positives in a high noise regime. The approach initially estimates mask for abnormal tissues based on reconstruction error in the high noise regime. Then an iterative method is applied to inpaint regions of the mask using information outside the mask in a lower noise regime.

The patched diffusion model (pDDPM) [13] performs the noising and denoising within a patch of the whole slice. That is the rest of the slice gives context for the DDPM of the noised patch. Versions of each slice with patches at different locations are used to identify abnormalities within the slice. In

a follow up work [21], a conditional DDPM (cDDPM) is used for denoising. The conditioning signal is the latent embedding from a masked auto-encoder (MAE) [47] pretrained on normal MRI slices, which is further fine-tuned during training. This conditioning gives the model global perspective of structure while performing the denoising.

VI. DISCUSSION

The results showcase that Patch2Loc advances the state of the art for unsupervised abnormality segmentation in neuroimages through an intuitive approach. Its promising performance meets or exceeds the best performing benchmark cDDPM [21], which has a more complicated structure for training and inference due to the combination of the masking autoencoder and DDPM model. In contrast, Patch2Loc is unique in terms of its dependence of local features, without global context, and it does not depend on reconstruction errors compared to the others. During test time, our method does not depend on hyperparameter such as the amount or type of noise added. For instance, DAE [33] has to search for the correlated noise parameter that gives the best performance. Generally, prior work requires extensive hyperparameter search during training and/or testing, especially for methods involving GANs. In contrast, Patch2Loc's hyperparameters are optimized for the normal anatomical structure of brain images from the IXI brain slices before the models (one for T1 and T2) are evaluated on different datasets.

One limitation of Patch2Loc is its ability to infer the correct location when abnormalities are smaller than the patch size. Smaller patches deteriorate prediction performance on normal patches, due to the high similarity of patches from widely different locations. This aleatoric uncertainty for the location prediction cannot be solved by changing the model. Thus, a possible solution to provide finer grained abnormality detection is to apply out-of-distribution detection on the latent representation of the model when it is still spatially organized. This can provide finer-grained within patch abnormality scores.

Another future research direction is to use 3D patches instead of 2D. This will change our model from being conditional on the slice location to being unconditional. We choose 2D slice since it mimics how practitioners look at the brain MRI images. Nonetheless, 3D patches can also enrich the model with more information since it gives the model the opportunity to learn the depth information instead of being conditioned on a small piece of it (i.e., the slice index).

VII. CONCLUSION

We have introduced Patch2Loc, a novel self-supervised learning task and model tailored for lesion detection in neuroimages, and demonstrated its effectiveness for unsupervised abnormal tissue segmentation. Our approach leverages the regularities of location-specific image features to identify abnormalities in brain tissues and directly incorporates uncertainty estimates using the β -NLL framework [16]. Unlike prior methods that focus on global features, Patch2Loc emphasizes local representations, enhancing its applicability to unsupervised abnormality segmentation in brain MRI. Our method does not need to any hyperparameter adjustment such as the added

noise during the inference time compared to state-of-the-art methods [13], [21] that rely on denoising diffusion models. This work introduces a new perspective on unsupervised abnormality segmentation in neuroimaging and lays the foundation for future research in this direction.

APPENDIX

The appendix contains additional figures referenced in the main body. Fig. 9 show kernel density estimates of the log-error and log-variance of normal and abnormal patches from the ATLAS, MSLUB, and WMH datasets. Figures 5, 6, 7, and 8 show slice, Patch2Loc’s heatmap, and ground truth for representative slices from each dataset.

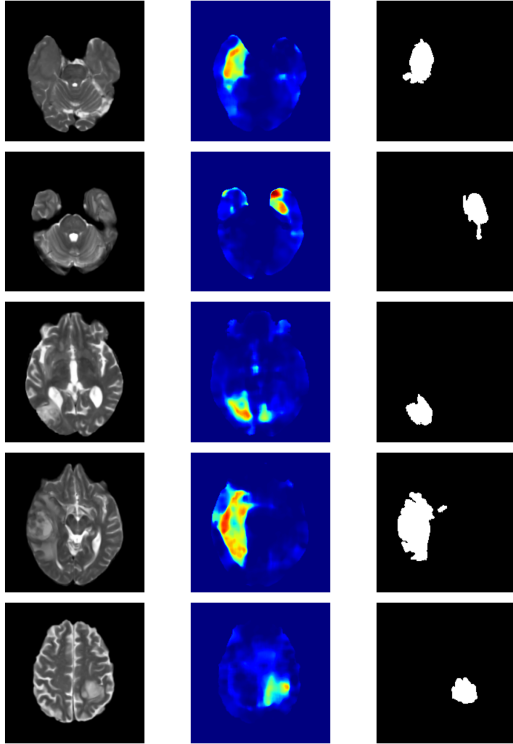


Fig. 5. Visualization of slices from BraTS. From left to right: the input slice, the heatmap (blue is low, red is the maximum), and the ground truth for abnormal tissues.

ACKNOWLEDGEMENTS

This research was supported in part through the use of Information Technologies (IT) resources at the University of Delaware, specifically the high-performance computing resources. The authors would like to thank Heidi Kecskemethy and Rahul Nikam from Nemours Children’s Hospital, and Sokratis Makrogiannis from Delaware State University for engaging discussions regarding computer-assisted neuroradiology.

REFERENCES

- [1] C. Josephson *et al.*, “Seizure risk with avm treatment or conservative management: Prospective, population-based study,” *Neurology*, vol. 79, pp. 500–507, 2012.
- [2] L. Merewitz and J. H. Sunshine, “A portrait of pediatric radiologists in the united states,” *American Journal of Roentgenology*, vol. 186, no. 1, pp. 12–22, 2006.

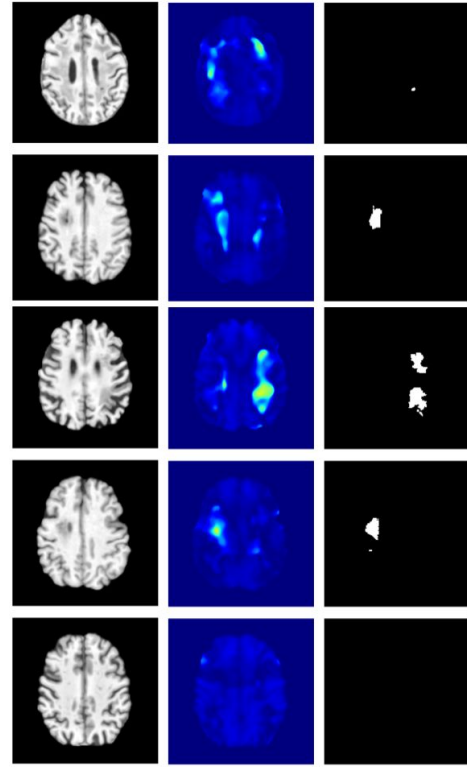


Fig. 6. Visualization of slices from ATLAS. From left to right: the input slice, the heatmap (blue is low, red is the maximum), and the ground truth for abnormal tissues

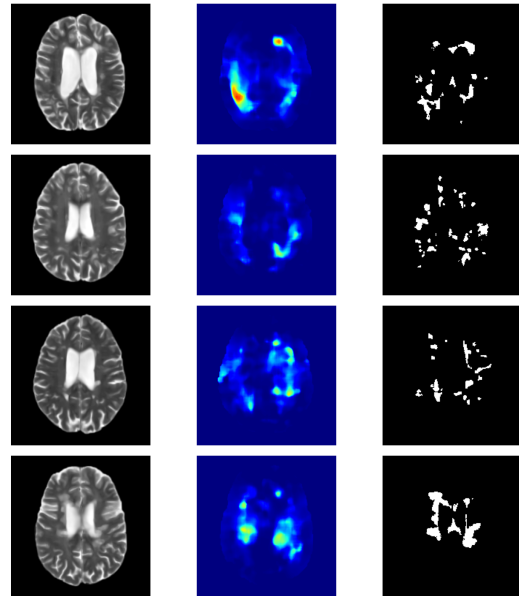


Fig. 7. Visualization of slices from MSLUB. From left to right: the input slice, the heatmap (blue is low, red is the maximum), and the ground truth for abnormal tissues.

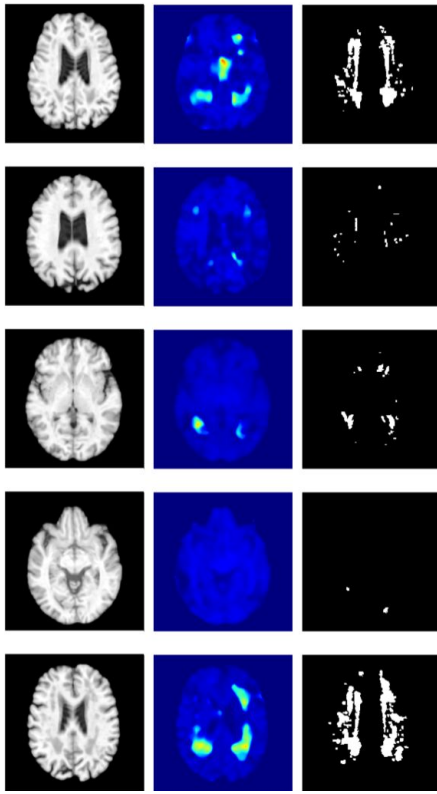


Fig. 8. Visualization of slices from WMH. From left to right: the input slice, the heatmap (blue is low, red is the maximum), and the ground truth for abnormal tissues

- [3] D. L. Kent, D. R. Haynor, W. Longstreth, and E. B. Larson, "The clinical efficacy of magnetic resonance imaging in neuroimaging," *Annals of Internal Medicine*, vol. 120, no. 10, pp. 856–871, 1994.
- [4] R. M. Dijkhuizen and K. Nicolay, "Magnetic resonance imaging in experimental models of brain disorders," *Journal of Cerebral Blood Flow & Metabolism*, vol. 23, no. 12, pp. 1383–1402, 2003.
- [5] S. N. Saleem, "Fetal magnetic resonance imaging (mri) a tool for a better understanding of normal and abnormal brain development," *Journal of Child Neurology*, vol. 28, no. 7, pp. 890–908, 2013.
- [6] X. Zhao and X.-M. Zhao, "Deep learning of brain magnetic resonance images: A brief review," *Methods*, vol. 192, pp. 131–140, 2021.
- [7] L. Busby, J. Courtier, and C. Glastonbury, "Bias in radiology: the how and why of misses and misinterpretations," *Radiographics*, vol. 38, p. 236, 2018.
- [8] M. Hagens *et al.*, "Impact of 3 tesla mri on interobserver agreement in clinically isolated syndrome: a magnims multicentre study," *Multiple Sclerosis Journal*, vol. 25, pp. 352–360, 2019.
- [9] J. Wyatt, A. Leach, S. M. Schmon, and C. G. Willcocks, "Anoddpn: Anomaly detection with denoising diffusion probabilistic models using simplex noise," in *Proceedings of the IEEE/CVF Conference on Computer Vision and Pattern Recognition*, 2022, pp. 650–656.
- [10] W. H. Pinaya *et al.*, "Fast unsupervised brain anomaly detection and segmentation with diffusion models," in *International Conference on Medical Image Computing and Computer-Assisted Intervention*. Springer, 2022, pp. 705–714.
- [11] W. Pinaya *et al.*, "Unsupervised brain imaging 3d anomaly detection and segmentation with transformers," *Medical Image Analysis*, vol. 79, p. 102475, 2022.
- [12] C. Bercea, B. Wiestler, D. Rueckert, and J. A. Schnabel, "Evaluating normative learning in generative ai for robust medical anomaly detection," 2023.
- [13] F. Behrendt, D. Bhattacharya, J. Krüger, R. Opfer, and A. Schlaefer, "Patched diffusion models for unsupervised anomaly detection in brain mri," in *Medical Imaging with Deep Learning*. PMLR, 2024, pp. 1019–1032.
- [14] C. I. Bercea, M. Neumayr, D. Rueckert, and J. A. Schnabel, "Mask, stitch, and re-sample: Enhancing robustness and generalizability in anomaly detection through automatic diffusion models," in *ICML 3rd Workshop on Interpretable Machine Learning in Healthcare (IMLH)*, 2023. [Online]. Available: <https://openreview.net/forum?id=kTpaPpXrqa>
- [15] D. A. Nix and A. S. Weigend, "Estimating the mean and variance of the target probability distribution," in *Proceedings of 1994 IEEE International Conference on Neural Networks (ICNN'94)*, vol. 1. IEEE, 1994, pp. 55–60.
- [16] M. Seitzer, A. Tavakoli, D. Antic, and G. Martius, "On the pitfalls of heteroscedastic uncertainty estimation with probabilistic neural networks," in *International Conference on Learning Representations*, 2022. [Online]. Available: <https://openreview.net/forum?id=aPOpXlnV1T>
- [17] K. He, X. Zhang, S. Ren, and J. Sun, "Deep residual learning for image recognition," in *Proceedings of the IEEE conference on computer vision and pattern recognition*, 2016, pp. 770–778.
- [18] A. Vaswani, "Attention is all you need," *Advances in Neural Information Processing Systems*, 2017.
- [19] T. Rohlfing, N. M. Zahr, E. V. Sullivan, and A. Pfefferbaum, "The SRI24 multichannel atlas of normal adult human brain structure," *Hum. Brain Mapp.*, vol. 31, no. 5, p. 798, Dec. 2009.
- [20] L. G. Nyul, J. K. Udupa, and X. Zhang, "New variants of a method of MRI scale standardization," *IEEE Trans. Med. Imaging*, vol. 19, no. 2, pp. 143–150, Feb. 2000.
- [21] F. Behrendt *et al.*, "Guided reconstruction with conditioned diffusion models for unsupervised anomaly detection in brain mris," *Computers in Biology and Medicine*, vol. 186, p. 109660, 2025.
- [22] B. H. Menze *et al.*, "The multimodal brain tumor image segmentation benchmark (brats)," *IEEE Transactions on Medical Imaging*, vol. 34, no. 10, pp. 1993–2024, 2014.
- [23] U. Baid *et al.*, "The rsna-asnr-miccai brats 2021 benchmark on brain tumor segmentation and radiogenomic classification," *arXiv preprint arXiv:2107.02314*, 2021.
- [24] Ž. Lesjak *et al.*, "A novel public mr image dataset of multiple sclerosis patients with lesion segmentations based on multi-rater consensus," *Neuroinformatics*, vol. 16, pp. 51–63, 2018.
- [25] H. J. Kuijff *et al.*, "Standardized Assessment of Automatic Segmentation of White Matter Hyperintensities and Results of the WMH Segmentation Challenge," *IEEE Trans. Med. Imaging*, vol. 38, no. 11, pp. 2556–2568, Nov. 2019.
- [26] S.-L. Liew *et al.*, "A large, curated, open-source stroke neuroimaging dataset to improve lesion segmentation algorithms," *Sci. Data*, vol. 9, no. 320, pp. 1–12, Jun. 2022.
- [27] D. P. Kingma and J. Ba, "Adam: A Method for Stochastic Optimization," *International Conference on Learning Representations*, 2014. [Online]. Available: <https://www.semanticscholar.org/paper/Adam%3A-A-Method-for-Stochastic-Optimization-Kingma-Ba/a6cb366736791bcccc5c8639de5a8f9636bf87e8>
- [28] F. Meissen, J. Paetzold, G. Kaissis, and D. Rueckert, "Unsupervised Anomaly Localization with Structural Feature-Autoencoders," *arXiv*, Aug. 2022.
- [29] F. Meissen, G. Kaissis, and D. Rueckert, "Challenging Current Semi-supervised Anomaly Segmentation Methods for Brain MRI," in *Brainlesion: Glioma, Multiple Sclerosis, Stroke and Traumatic Brain Injuries*. Cham, Switzerland: Springer, Jul. 2022, pp. 63–74.
- [30] F. Behrendt, M. Bengs, D. Bhattacharya, J. Krüger, R. Opfer, and A. Schlaefer, "Capturing Inter-Slice Dependencies of 3D Brain MRI-Scans for Unsupervised Anomaly Detection," *OpenReview*, Apr. 2022. [Online]. Available: <https://openreview.net/forum?id=db8wDgKH4p4>
- [31] C. I. Bercea, B. Wiestler, D. Rueckert, and J. A. Schnabel, "Reversing the abnormal: Pseudo-healthy generative networks for anomaly detection," *arXiv preprint arXiv:2303.08452*, 2023.
- [32] C. Baur, S. Denner, B. Wiestler, N. Navab, and S. Albarqouni, "Autoencoders for unsupervised anomaly segmentation in brain mr images: a comparative study," *Medical Image Analysis*, vol. 69, p. 101952, 2021.
- [33] A. Kascenas, N. Pugeault, and A. Q. O'Neil, "Denoising autoencoders for unsupervised anomaly detection in brain mri," in *International Conference on Medical Imaging with Deep Learning*. PMLR, 2022, pp. 653–664.
- [34] C. I. Bercea, B. Wiestler, D. Rueckert, and J. A. Schnabel, "Generalizing Unsupervised Anomaly Detection: Towards Unbiased Pathology Screening," Apr. 2023, [Online; accessed 2 Jun. 2025]. [Online]. Available: <https://openreview.net/forum?id=8ojx-Ld3yJR>
- [35] I. J. Goodfellow *et al.*, "Generative adversarial nets," *Advances in neural information processing systems*, vol. 27, 2014.
- [36] D. Zimmerer, S. A. Kohl, J. Petersen, F. Isensee, and K. H. Maier-Hein, "Context-encoding variational autoencoder for unsupervised anomaly detection," *arXiv preprint arXiv:1812.05941*, 2018.

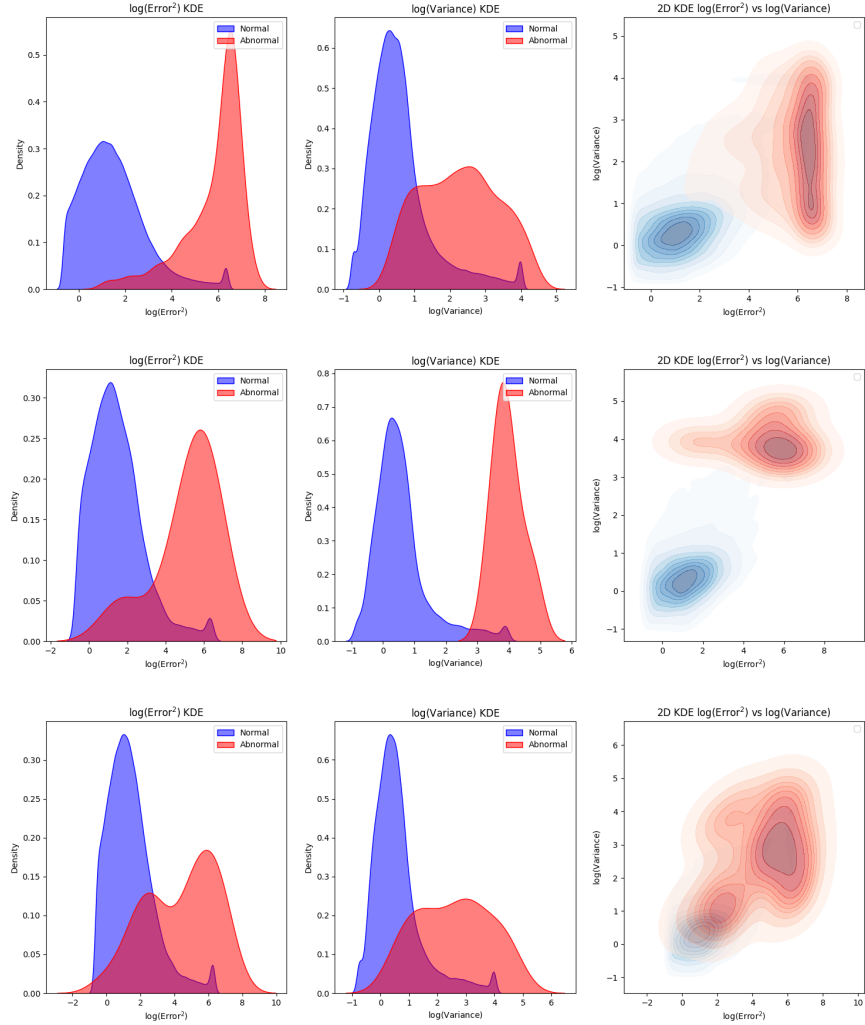


Fig. 9. From left to right: 1D KDE for log-error, and log-variance, and 2D KDE for log-error and log-variance for normal patches (blue) and abnormal patches (red). Top to bottom: ATLAS, MSLUB, and WMH datasets.

- [37] K. Sato, K. Hama, T. Matsubara, and K. Uehara, “Predictable uncertainty-aware unsupervised deep anomaly segmentation,” in *2019 International Joint Conference on Neural Networks (ijcnn)*. IEEE, 2019, pp. 1–7.
- [38] X. Chen and E. Konukoglu, “Unsupervised detection of lesions in brain mri using constrained adversarial auto-encoders,” *arXiv preprint arXiv:1806.04972*, 2018.
- [39] C. Baur, B. Wiestler, S. Albarqouni, and N. Navab, “Deep autoencoding models for unsupervised anomaly segmentation in brain mr images,” in *Brainlesion: Glioma, Multiple Sclerosis, Stroke and Traumatic Brain Injuries: 4th International Workshop, BrainLes 2018, Held in Conjunction with MICCAI 2018, Granada, Spain, September 16, 2018, Revised Selected Papers, Part I 4*. Springer, 2019, pp. 161–169.
- [40] X. Chen, S. You, K. C. Tezcan, and E. Konukoglu, “Unsupervised lesion detection via image restoration with a normative prior,” *Medical Image Analysis*, vol. 64, p. 101713, 2020.
- [41] K. Van Hespén, J. Zwaneburg, J. Dankbaar, M. Geerlings, J. Hendrikse, and H. Kuijf, “An anomaly detection approach to identify chronic brain infarcts on mri,” *Scientific Reports*, vol. 11, pp. 1–10, 2021.
- [42] A. Taleb *et al.*, “3d self-supervised methods for medical imaging,” in *Advances in Neural Information Processing Systems*, H. Larochelle, M. Ranzato, R. Hadsell, M. F. Balcan, and H. Lin, Eds., vol. 33. Curran Associates, Inc., 2020, pp. 18 158–18 172. [Online]. Available: <https://proceedings.neurips.cc/paper/2020/file/d2dc6368837861b42020ee72b0896182-Paper.pdf>
- [43] C. Doersch, A. Gupta, and A. A. Efros, “Unsupervised visual representation learning by context prediction,” in *Proceedings of the IEEE international conference on computer vision*, 2015, pp. 1422–1430.
- [44] J. Sohl-Dickstein, E. Weiss, N. Maheswaranathan, and S. Ganguli, “Deep unsupervised learning using nonequilibrium thermodynamics,” in *International conference on machine learning*. pmlr, 2015, pp. 2256–2265.
- [45] J. Ho, A. Jain, and P. Abbeel, “Denoising diffusion probabilistic models,” *Advances in neural information processing systems*, vol. 33, pp. 6840–6851, 2020.
- [46] Z. Liang, H. Anthony, F. Wagner, and K. Kamnitsas, “Modality cycles with masked conditional diffusion for unsupervised anomaly segmentation in mri,” 2023.
- [47] K. He, X. Chen, S. Xie, Y. Li, P. Dollár, and R. Girshick, “Masked autoencoders are scalable vision learners,” in *Proceedings of the IEEE/CVF conference on computer vision and pattern recognition*, 2022, pp. 16 000–16 009.